

A representative airglow volume emission profile from rocket-borne photometer data by an artificial neural network technique

F.C. de Meneses¹, E.H. Shiguemori², P. Muralikrishna³ and B.R. Clemesha³

Manuscript received on October 21, 2010 / accepted on August 30, 2011

ABSTRACT

The inverse problem to retrieve useful airglow volume emission rate profiles from rocket-borne photometer measurements has been solved by adopting the well-characterized spectral photometric methods. An alternative recovery method based on artificial neural network (ANN) is presented. A multilayer perceptron neural network was trained with available experimental and synthetic data. Integrated emissions profiles measured by a rocket experiment were taken as the input data. From the results obtained in this work, it may be concluded that the ANN technique is a convenient tool to recover volume emission rate profiles.

Keywords: applied computing in space and environmental sciences, neural networks, inverse problem, airglow, rocket.

1 INTRODUCTION

The airglow phenomenon can be defined as a spontaneous emission of light from a planetary atmosphere in the range of wavelength from the far UV to near IR. Like the auroras, the airglow is also caused by excitation of the upper atmospheric constituents, however, the auroral excitation mainly occurs by collisions with precipitating energetic particles of the solar wind, whereas short-wavelength solar photons produce excitation through photochemical processes giving rise to the airglow emission. Unlike the auroras that are geographically confined to the region surrounding the geomagnetic poles and sporadically observed in middle and low latitudes during geomagnetic storm events, the unstructured airglow emission covers all latitude range, although indiscernible with unaided eyes [1, 2].

This nonthermal luminescence results from discrete atomic and molecular transitions of the constituents of the atmosphere

and thus has in the spectrum an associated emission line/band [3]. Measurements of airglow emission on the Solar System planets have proved a useful tool in studying the behaviour of the ionosphere and the upper atmosphere, primarily on the dynamical-photochemical processes that control the species composition and energy balance [4, 5, 6].

In this work we will focus on the mesospheric component of the atomic oxygen OI 557.7 nm airglow emission, called green line, produced by a forbidden transition from the O(¹S) to the O(¹D) level. The OI 557.7 nm airglow emission comes from two sources, one from the thermosphere located at about 250 km altitude and the other from around 97 km, in the upper mesosphere [7]. The thermospheric component of OI 557.7 nm intensity is usually very weak or virtually nonexistent except at equatorial latitudes [8]. Integrated intensity measurements of the OI 557.7 nm have been used often to study the mesospheric oxygen concentration [9, 10, 11].

Correspondence to: F.C. de Meneses

¹State Key Laboratory of Space Weather, Center for Space Science and Applied Research (CSSAR), CAS, Beijing, P.R. China

²Instituto de Estudos Avançados (IEAv), São José dos Campos, SP, Brazil

³Instituto Nacional de Pesquisas Espaciais (INPE), São José dos Campos, SP, Brazil

E-mails: xico@spaceweather.ac.cn / elcio@ieav.cta.br / murali@dae.inpe.br / brc@laser.inpe.br

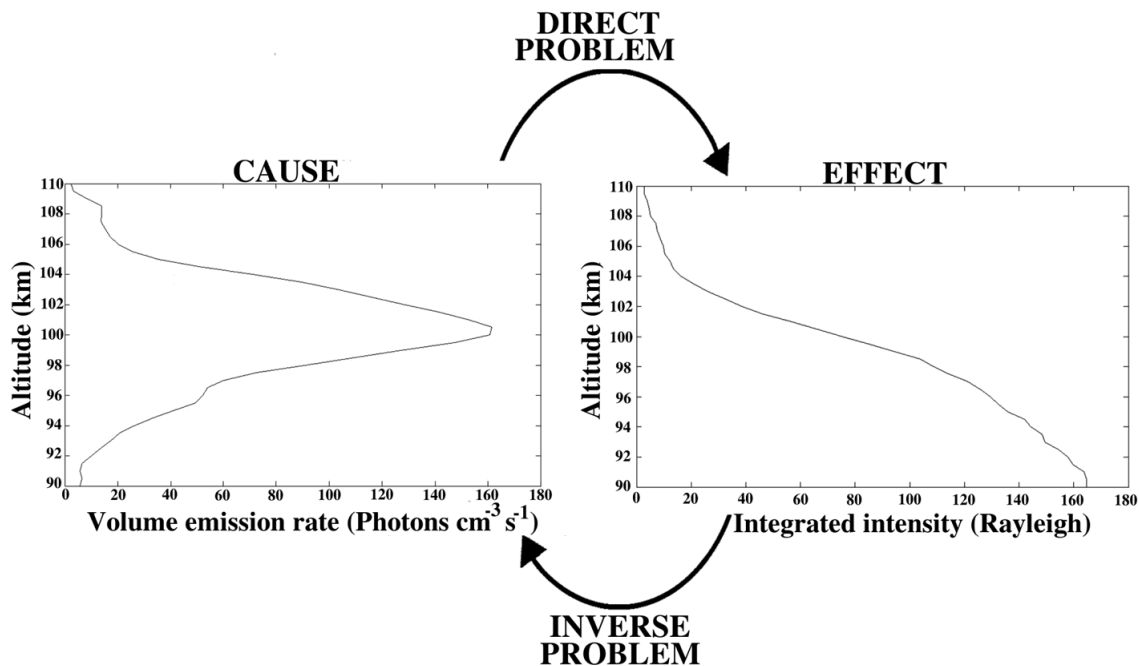


Figure 1 – The inverse problem is the determination of the volume emission rate profile (left) from integrated emission intensity profile (right). This paper presents a method to solve the inverse problem by ANN.

On the respective emitting layer, the green line volume emission rate (in photons $\text{cm}^{-3} \text{s}^{-1}$) is assumed to be horizontally uniform over the field of view, while the signal measured by a photometer, named integrated emission, corresponds to the number of photons emitted per second from a column of cross-section oriented along the line of sight. This photometric quantity is measured in Rayleigh units [12].

Ground based OI 557.7 nm airglow measurements do not provide layer altitude information directly, so integrated rocket *in-situ* measurements of airglow emissions make it possible to infer volume emission rate profiles. Currently, there are few data available about rocket experiments to investigate the airglow emissions from the equatorial and low latitude regions, unlike the middle and high latitudes [13].

The photometer signal variations during the period when it is looking for the airglow emission layer contain information on its integrated emission. This signal can be inverted to obtain the vertical emission profile (Fig. 1), taking into account, during the inversion process, the concern to preserve as much as possible the information contained in aeronomically important structures found in the raw data [14]. In practice, inversion of the integrated signal is an ill-posed inverse problem to recover the emission rate vertical profile in accordance with the photometer mounting on the payload as well as the rocket attitude along its trajectory.

In photometric remote sensing, some traditional methods have been often applied to derive the volume emission rate profiles from integrated emission measurements, e.g., a method of incremental straight line fitting [14], Fourier filtering [15] and an onion-skin type analysis [16]. However, the classical spectral imaging methods generally involve loss of information as a result of input data manipulation and require complicated inversion techniques. Instead, an alternative method based on observational empirical knowledge would be tested. An artificial neural network (ANN) technique based on training a set of multilayer perceptrons is applied to solve the inversion problem of OI 557.7 nm airglow profile retrieval from rocket *in-situ* measurements of integrated emissions. In order to recognize patterns, an ANN seeks to capture the functional relationship between input-output data, learning from the examples presented. Hence, it doesn't need a mathematical model associated with the inverse problem, mostly ill-conditioned.

ANN have been successfully employed for short-term prediction of ionospheric parameters [17, 18, 19, 20, 21], and are useful tools to provide model parameters for the lower ionosphere [22, 23]. Applications involving space weather can also be found in the literature [24, 25]. Neural networks offer a number of advantages, as the ability to apprehend implicit non-linear relationships between input and output variables [26],

fault-tolerance and generalization capability [27]. Although one can determine the architecture and topology of the network, the user can not follow the progress of the learning process interactively, which constitutes a major disadvantage. Moreover, in practice, the ANN bears some pitfalls, which can be bypassed when there is awareness about them. According to [28], the lack of an uniform heuristic in building ANN models and its nonlinear non-parametric nature contribute largely to provide several common pitfalls in neural network applications.

The purpose of the present work is to compare green line volume emission rate profiles obtained from ANN with those provided by the method of incremental straight line fitting. In both methods, integrated emission input data are derived from a sounding rocket experiment carried out in Alcântara, Brazil.

2 THE ROCKET EXPERIMENT

Mounted in a bay below the rocket nose cone, the MULTIFOT airglow photometer payload was launched from equatorial station Alcântara (2.5°S, 44.4°W) on-board a reduced version of a SONDA III Brazilian rocket at 23:52 (Local Time) on 31 May 1992, and reached an apogee of 282 km covering a ground range of 398 km. This payload of 105 kg included a OI 557.7 nm forward-looking photometer, the data collected from which will be examined in this work. Photometer signals were recorded in a 10 bit word at a sample rate of 250 s⁻¹ prior to being telemetered to the ground tracking station. The rocket and the launch facilities were provided, respectively, by Brazilian Institute for Space and Aeronautics (IAE/DCTA) and Alcântara Launching Center (CLA), while the scientific payload and the telemetry systems were developed at the National Institute for Space Research (INPE). A detailed discussion about the complete airglow photometer payload and operation of the experiment can be found in [13].

3 DIRECT PROBLEM

Since the OI 557.7 nm airglow emission is confined to a certain high interval, the fundamental quantity to be measured is the volume emission rate ϵ , which is characterized by the number of photons emitted per second from a unit volume. However, this quantity cannot be measured directly.

In the forward-looking photometer configuration, the field of view is aligned with the axis of the rocket. Below the height of emission layer, the photometer continuously measures the OI 557.7 nm emission, while above the layer it looks out into space. Assuming that the emission is horizontally uniform over the field of view, the photon rate collected from a column by a ground

photometer with area A in a time unit is the integral along the line of sight from the length of the rocket (h_o) to the maximum height of layer (h_{max}):

$$I = \frac{1}{10^6} \int_{h_o}^{h_{max}} \epsilon(h) dh, \quad (1)$$

usually called integrated emission. Its radiometric unit in SI, Rayleigh, corresponds to the emission of 10⁶ photons cm⁻² s⁻¹ from a column of one square centimeter in area extending along the line of sight in any direction through the emitting region [12]. Equation 1 represents the mathematical formulation of the direct problem. In the subsequent steps in this methodology of ANN, the solution of the direct problem will be applied to generate a portion of the training set.

4 NEURAL NETWORK ARCHITECTURE

An artificial neural network was employed to reproduce a nonlinear relation between integrated emission measurements performed along the height and a volume emission rate vertical profile, where the input space corresponds to certain parameters which play a dominant role in the desired output profile. The input parameters were the integrated emission intensity I (in Rayleigh), zenith angle θ (in degrees), and rocket altitude h (in km). The angle θ is derived from both on board magnetometer and a side-looking photometer data by calculating the rocket attitude, while the altitude h is determined from data collected by a tracking radar. Each set of three input values univocally corresponds to only one output point. A schematic diagram of ANN is shown in Figure 2.

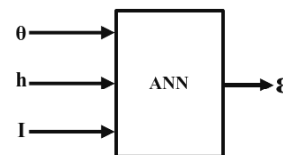


Figure 2 – An input-output schematic diagram of ANN, where the input parameters are the zenith angle θ , rocket altitude h and integrated emission intensity I measured at different altitudes throughout the flight. The output is a value of volume emission rate ϵ corresponding to the respective altitude.

The choice of these parameters is based on the argument that to derive volume emission profiles from the integrated emission intensities measured by a forward-looking photometer at different altitudes throughout the flight, it is also necessary to provide information about the zenith angle of the photometer field of view (FOV), which varies continuously due to the rocket precession and the effects of aerodynamic drag. In the case of a forward-looking photometer, the FOV is not influenced by the rocket spin.

The input data presented to the network cover a grid of altitude between 90 and 110 km in steps of 0.5 km intervals, while the zenith angles are as follows: 0°, 10°, 20°, 30°, 35° and 40°. A range of zenith angle closer to reality would require a detailed interpolation between the values presented above, which would result in a huge number of profiles to be implemented during the training stage. It was verified that when this occurs, the network falls into local minimum point and it can not perform the training required. The intrinsic properties of ANN that make it insensitive to loss and failure of some of the elements of the range, allows us to take just 6 zenith angle values without loss of generalization in the results.

Basically, a neural network is composed of a set of nonlinear processing units called neurons, which processes the input signal received as a nonlinear combination followed by levels of activation, which in turn depend on the outcome of this combination (Fig. 3).

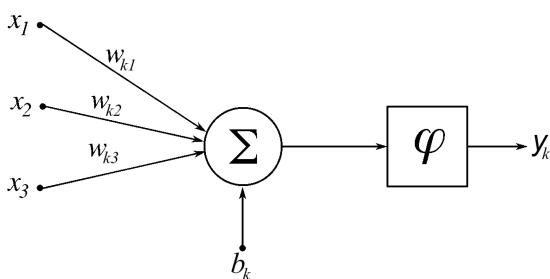


Figure 3 – A computational approach of a single neuron structure. The bias is shown below the logic unit with sigma function and the weights alongside the neural connections.

A logic unit calculates the weights between an input and a neuron, reflecting the character either excitatory or inhibitory of the connections. The sum of the product $w_{kj} x_j$ is biased b_k towards a nonlinear function φ , scaling the output to a determined range of values. A model of neuron is mathematically described by

$$y_k = \varphi \left(\sum_{j=1}^n w_{kj} x_j + b_k \right), \quad (2)$$

where w_{kj} are the connection weights, b_k is a bias parameter, x_j is the input vector and y_k is the output of the k^{th} neuron. The $\varphi(\cdot)$ is the function that provides the activation for the neuron. A sigmoid function is adopted here as an activation function [29].

Each neuron that forms an ANN by inter-connections has just one output, which will be multiplied by a weight if applied as the input to a next neuron. Therefore, a basic network topology consists of an input node layer, one or more hidden layers,

and one output layer. By connections, the information is passed from the input nodes to the neurons in the hidden layer which, in turn, passes them to the output layer units. The number of neurons in the hidden layer is determined iteratively during the training stage.

The network adopted in this work was a Multilayer Perceptron (MLP) with backpropagation algorithm [30], which exhibits a single layer of hidden neurons and nonlinear activation. It was implemented using a code in Fortran 90 instead of standard ANN toolboxes and packages available everywhere. The advantage of this choice is that it allows us to create a heuristic that enhances a wide interaction with the network architecture and topology.

Figure 4 shows the network architecture adopted containing three input nodes, one hidden layer and an output neuron. The backpropagation is a supervised learning method designed to minimize the error between the output calculated by the network (y_j) and the desired output (d_j) estimated for any given input. This operation requires the presentation of a set constituted by the pair: input profile and output desired profile as response to the input. Both output profiles are compared. The network global error is computed from this comparison. The weights are adjusted by an amount proportional to the global error. The Equation (3) shows the general weight correction according to the so-called delta rule [29], a gradient descent learning rule for updating the weights given by

$$\Delta w_{kj} = \eta \delta_k y_j, \quad (3)$$

where η is the learning rate parameter that controls the strength of change, δ_k is the local gradient, which depends on whether neuron k is in the output or hidden layer, and y_j is the input signal of a neuron k . For further details regarding the ANN architectures and algorithms, see [30].

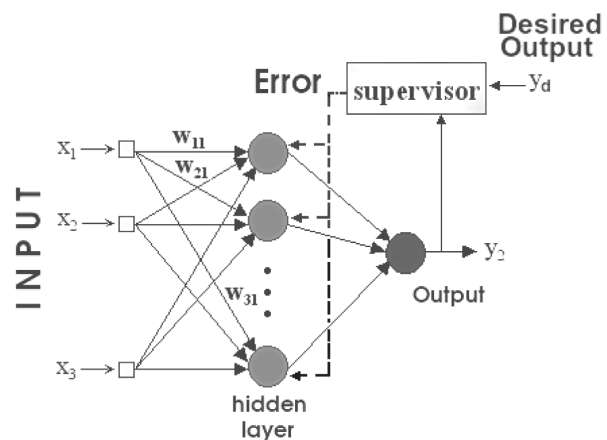


Figure 4 – Supervised backpropagation feed-forward multilayer neural network.

Table 1 – Geophysical data between Alcântara and Natal for the days 31 May 1992 and 11 Dec. 1985, respectively. The geophysical conditions are represented by the planetary indices ΣK_p and A_p and the daily index of 10.7-cm wavelength solar radio flux.

Alcântara (2.5°S, 44.4°W)	Natal (5.8°S, 35.2°W)
31 May 1992, 23:52 (LT)	11 Dec. 1985, 20:30 (LT)
$\Sigma K_p = 15$	$\Sigma K_p = 18.7$
F10.7 cm solar flux = 101.4	F10.7 cm solar flux = 77.3
$A_p = 7.75$	$A_p = 7.0$

An optimum architecture is found by the response on each attempt of the ANN trained with various combinations of characteristics of a perceptron network, like the learning rate, number of epochs to achieve a desired error and number of neurons in the hidden layer(s). The latter is especially important in light of the training capacity, because when an inadequate number of neurons is chosen, the network does not achieve a satisfactory training. When few neurons are used, the output is poor and unrepresentative, whereas an excessive number of neurons, apart from increasing the training time, may cause overtraining.

5 TRAINING AND TESTING

While using an ANN, two phases can be devised: the training and activation phases. The training process starts with the weights and bias chosen randomly. They will be updated after each iteration n by the action of the backpropagation algorithm via minimization of the error between the desired (d_j) and network (y_j) outputs for a neuron j , defined by

$$E(n) = \frac{1}{2N} \sum_{n=1}^N [d_j(n) - y_j(n)]^2, \quad (4)$$

where N is the total number of patterns contained in the training subset.

Since a representative data set describing the history of the relationship between the input and output parameters is an essential requirement for training a network with good generalization and extrapolation abilities [23], there was an initial limitation in our database that needed to be circumvented. This limitation is as follows: OI 557.7 nm vertical profiles derived from rocket measurements in the equatorial region are scarce. This lack of information can not be compensated by abundant data from ground-based photometers, since this technique provide only integrated information about the airglow emission layer. Assuming that, for the season (autumn equinox) and band of

coordinates in question (around 2.5°S, 44.4°W), vertical profiles of OI 557.7 volume emission rate are not available, we consider two OI 557.7 nm profiles from a campaign conducted from Natal (5.8°S, 35.2°W), Brazil, on December 11, 1985 at 20:30 (Local Time), to build a learning set. From this poor sample set, we modeled more 1382 additional profiles, which incorporate theoretical constraints and variability features of experimental volume emission rate profiles. Despite the seasonal and geographical differences between Alcântara and Natal data, both types of profiles have some similarities in terms of geophysical conditions, as can be seen in Table 1.

The 30 most representative volume emission rate profiles were selected among the 1384 vertical profiles. These 30 profiles ε form the learning database, followed by their respective integrated emission intensities I derived from the solution of the direct problem. The resulting integrated intensities represent the forward-looking photometer measurements at different altitudes and the FOV zenith angle equal to zero. However, throughout a rocket flight, the zenith angle varies continuously. In this case, the intensity measured at any given height depends on the zenith angle, because of its direct relation with the optical path length. Since it is necessary to provide this information to the network, we determine the integrated intensities corresponding to the angles 0°, 10°, 20°, 30°, 35° and 40° by the expression $I = I_o V(h | \theta)$ that uses the van Rhijn function given by

$$V(h | \theta) = \frac{1}{\{1 - [R_T/(R_T + h)]^2 \sin^2 \theta\}^{1/2}}, \quad (5)$$

where I_o is the integrated intensity measured with the zenith angle $\theta = 0$, R_T is the Earth's radius and h is the height of rocket from the ground surface [3]. Thus, the database now has a total of 180 integrated emission profiles corresponding to the measurements of the 30 profiles of volume emission rate by the 6 different zenith angles.

Aiming to ensure the statistical uniformity of the data, not only the network input data, but also the complete database were normalized. Experimental errors during the measurements of integrated emission intensity were simulated by adding a random perturbation to the exact solution of the direct problem I , such that

$$\tilde{I} = I + I \sigma \mu, \quad (6)$$

where $\sigma=0.05$ is the standard deviation of the noise and μ is a random variable taken from a Gaussian distribution, with zero mean and unitary variance.

For training exclusively and testing purposes, the available database is then randomly divided into training, validation and generalization subsets, where each subset contains 1/3 of the total database. The need for this split can be explained as follows: the network should be trained to be able to learn enough from the training subset data, but also be able to generalize the results when new data are introduced. Therefore, in order to prevent the training results evolve toward a very particular section of the data (over-training), the network was optimized by a cross-validation test, where profiles from the validation subset are, once in an epoch, showed to the network and compared with the training results.

The comparison between the mean square errors of training and validation profiles is a convergence criterion, because the weight adjustment will stop as soon as the error on the cross validation set is higher than it was in the last check. Generally, the cross-validation error reached a minimum before the training error. The final weights and bias are fixed in this epoch. From this point there is no effect on weight adjustment.

As we see in Figure 5, the rms error is given as a function of the number of epochs for the training (solid line) and validation subsets (dashed line). After 42 epochs, the error of both drops sharply. The validation error becomes stable just prior to the training error. According to [31], the fact that the validation error remains approximately stable after reaching its minimum is an indication that the network is not over-fitting the training subset.

After the activation of the ANN, a critical analysis of its performance is made using the weights and bias obtained reaching the convergence. The effective test is conducted employing the generalization subset containing a population of 60 profiles, which have no relation with the validation and training subsets. The accomplishment of this test allows to verify if the network suffers from either underfitting or overfitting, as well as to find the best set of network topology as follows: 3 neurons in the hidden layer, learning rate equals to 0.5 and desired error equal to 1.0

$\times 10^{-4}$, where the number of epochs to reach the desired error safely was 1.0×10^5 . The results presented here are derived from this ANN topology.

The capacity of generalization of ANN can also be expressed by the root mean square (rms) error, which provides the square root of the mean error produced by the ANN, when a particular input data from generalization subset is presented to the network. The rms error is expressed by the following equation

$$E_{rms} = \sqrt{\frac{1}{N} \sum_{i=1}^N (y_{gen} - y_{ann})^2}, \quad (7)$$

where N is the number of testing data from the generalization subset. The volume emission rate data y_{gen} and y_{ann} are from, respectively, the generalization subset and ANN result. Along the range of altitude, the rms error over the entire subset is shown in Figure 6. We can see that the capacity of generalization is reasonably good, except between 95.5 km and 100 km. Predictions in this interval should be reported as suspicious. Therefore, by this information, we can realize that our training subset for this region is either poor of samples or unrepresentative, i.e, the profiles in this altitude range do not represent well the physical reality. This, as we see it, is an important detail that should be taken into account and improved in future works.

Figure 7 illustrates the skill of the network to retrieve volume emission rate profiles employing the generalization. The generalization subset provides both the integrated intensity profiles that will be inverted by the ANN and volume emission profiles that will be compared with those resulting from the network output. The coefficient of determination (R^2) gives the proportion of the variance of one profile from the other, allowing us to quantify how certain the ANN can be in making predictions. The plot on the left side of the Figure 7 shows the worst result of the test, where $R^2 = 0.7517$, while on the right side, the coefficient $R^2 = 0.9798$ indicates that both profiles agree quite well. The introduction of a random perturbation to the exact solution of the direct problem I , makes it difficult to match the fine details between the output and generalization profiles.

6 INVERSION EXPERIMENT

Now we will implement the ANN in order to derive vertical volume emission profiles from integrated emission intensity profiles. The inversion operation is performed to the MULTIFOT rocket measurements obtained both during the upleg and downleg portions. Therefore, the ANN input data comprise the integrated emission intensity I provided by the green line forward-looking

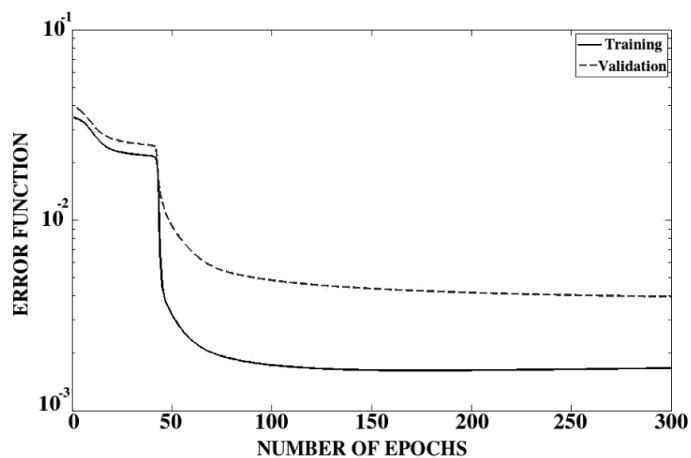


Figure 5 – The solid and dashed lines show, respectively, the rms error for the training and validation as a function of the number of epochs during the best training session.

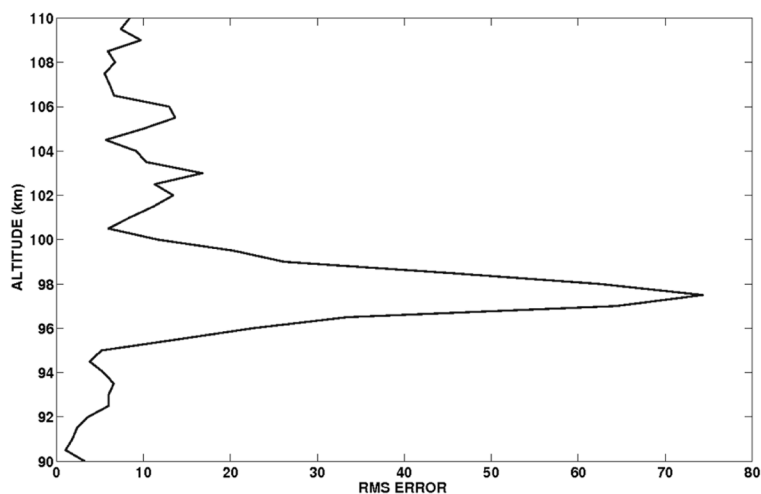


Figure 6 – The rms error between the volume emission rate data y_{gen} and y_{ann} along the altitude range.

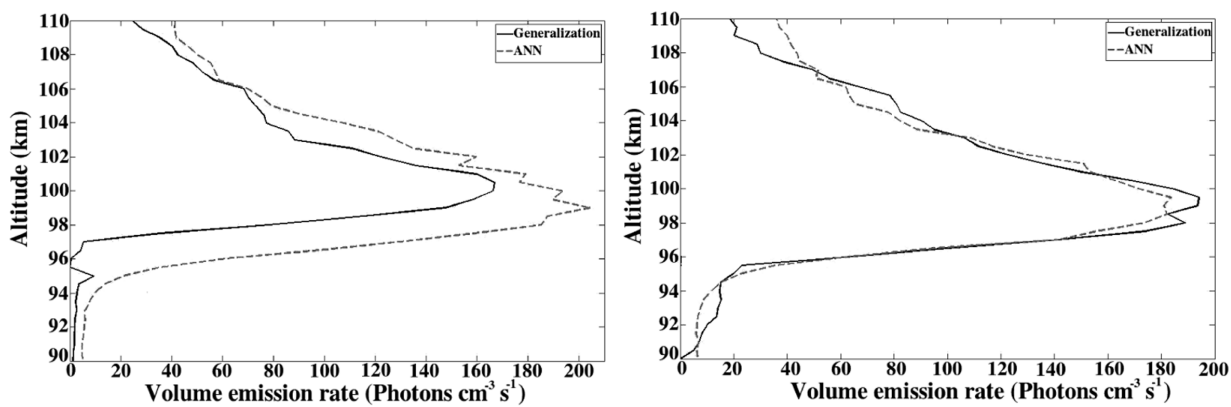


Figure 7 – The generalization test to check the performance of the ANN by comparison between volume emission rate profiles from generalization subset and ANN output. The plot on the left side shows the worst result of the test, while the one, on the right side, shows the best agreement obtained.

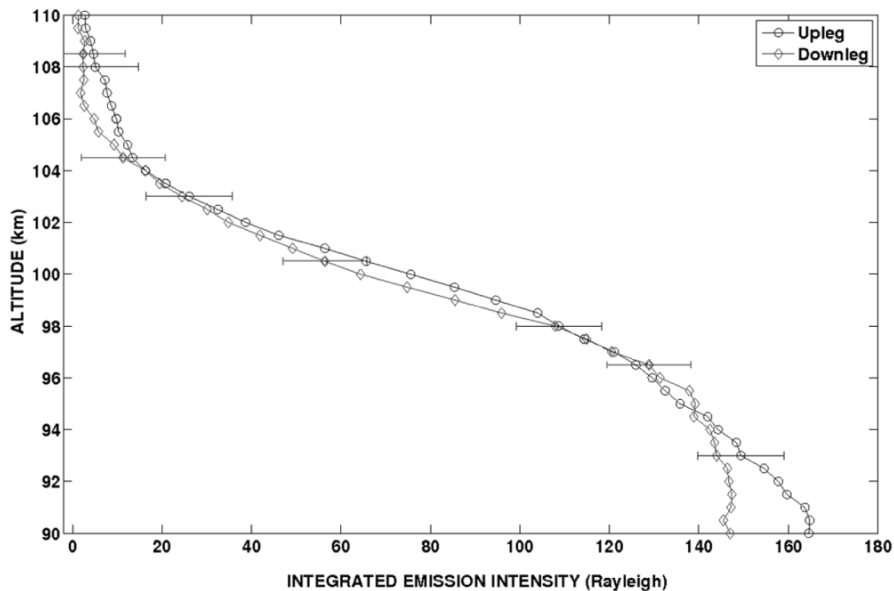


Figure 8 – Vertical profiles of integrated emission intensities measured by the MULTIFOT green line airglow photometer, along the upleg (circle line) and downleg (diamond line) portions.

photometer, the rocket axis zenith angle θ and the altitude h corresponding to these data. Figure 8 shows the two input profiles of integrated emission intensity measured by the green line forward-looking photometer on both upleg and downleg trajectories. The error bars in both profiles quantify the average standard deviation of samples.

After activating the network with an input pattern provided by the MULTIFOT data, one recovers vertical volume emission rate profiles (upleg and downleg) from the output of the ANN. The results shown in Figures 9 and 10 demonstrate the feasibility of this inversion method. Both profiles are also compared to their analogues derived by incremental straight line fitting method, a technique widely used to determine volume emission profiles from airglow integrated intensity measurements. This technique was previously applied to the OI 557.7 nm MULTIFOT data by [13] to 400 point data samples, corresponding to a fitting length of 3 km. The error bars in both figures represent the standard error of the estimate in the respective methods applied to obtain the volume emission profiles.

Figure 9 presents a comparison between upleg profiles obtained by incremental fitting technique (circle line) and ANN (diamond line). While the first method gives a peak value of $161.5 \text{ photons cm}^{-3} \text{ s}^{-1}$ at 100.5 km with a half-width of 5.96 km, in the second one, these values are $160.3 \text{ photons cm}^{-3} \text{ s}^{-1}$ at 99.5 km and half-width of 6.38 km.

Similarly, in Figure 10, the downleg profile derived by incremental fitting technique (circle line) shows a peak of $184.5 \text{ photons cm}^{-3} \text{ s}^{-1}$ at 99 km with a half-width of 6.45 km. In its analogue derived by ANN (starry line), we found a peak of $149.5 \text{ photons cm}^{-3} \text{ s}^{-1}$ at 99.5 km and a half-width of 6.45 km.

The similarity between profiles obtained by unrelated methods once again reinforces how realistic are the results presented by the ANN. However, it is precisely the marked difference between the recovery methods that is the source of discrepancies between the resulting profiles. We could enumerate the advantages and shortcomings of the recovery methods, which give results with a certain degree of similarity, but there is still some difficulty to define in absolute terms which one retrieves a profile actually not so far from the reality. The degree of universality, i.e., the range of circumstances where it may be applied, has not been well defined.

From the values found for the peak altitudes, we note that the height in both ANN profiles is invariant, while those provided by incremental fitting method show a variation of 1 km between upleg and downleg profiles. In this sense, it is interesting to remember a work, where [14] applied various techniques to derive volume emission profiles from rocket measurements of integrated emissions. Among them, incremental straight line fitting proved to be most suitable in most cases analyzed, but with a disadvantage: the altitude of peak emission can be ill-defined by an

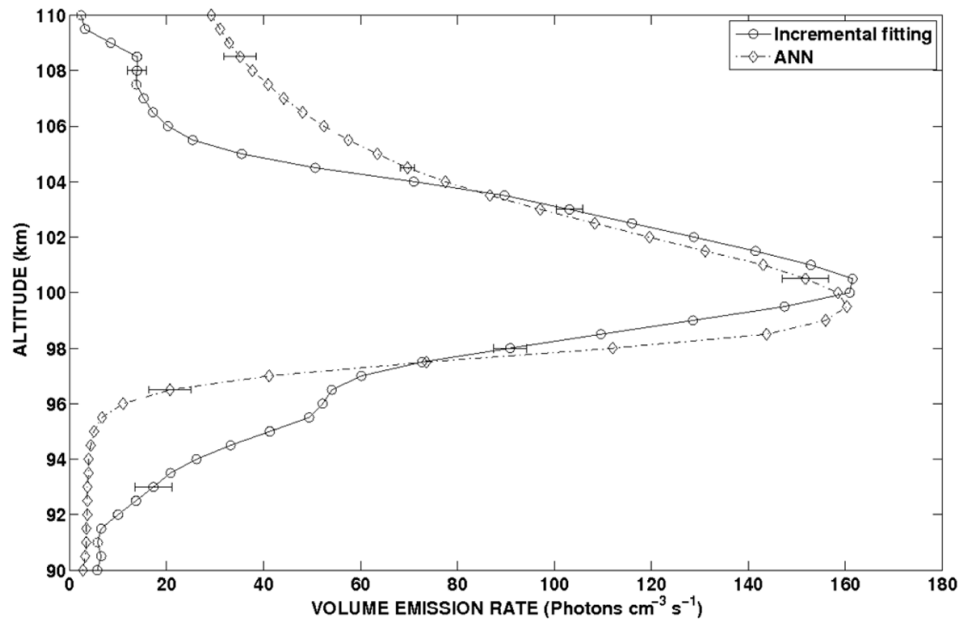


Figure 9 – Comparison between OI 557.7 nm volume emission rate profiles (upleg) obtained by incremental fitting technique (circle line) and ANN (diamond line) from the same data of integrated intensity.

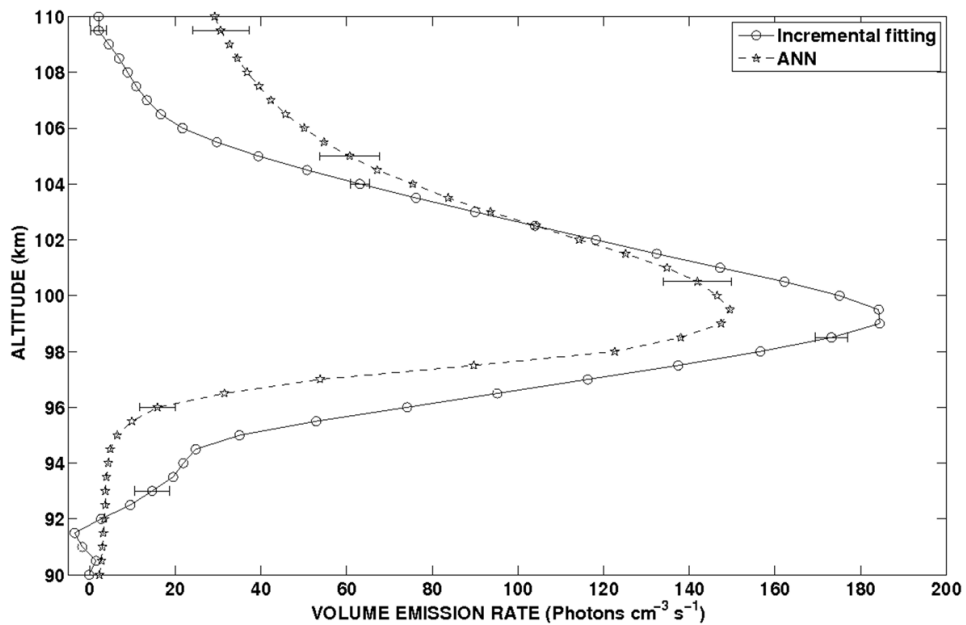


Figure 10 – Comparison between OI 557.7 nm volume emission rate profiles (downleg) obtained by incremental fitting technique (circle line) and ANN (starry line) from the same data of integrated intensity.

amount determined by point to point noise propagation. Therefore, regarding the height of the peaks, profiles obtained by incremental fitting method have no right to claim any prerogative over ANN results. Nevertheless, it is interesting to remember that this range of altitude is precisely that flagged as suspicious according to the analysis of Figure 6.

With respect to the volume emission rate values corresponding to peaks, we can easily see that they are very close to each other in the case of upleg profiles. However, the same is not true for the downleg profiles. Apart from the difference of 20% between the values obtained for the downleg profiles using these two different inversion techniques, the behaviour of the ANN

downleg profile intensity is, with respect to its equivalent in the upleg plot, precisely the opposite of what occurs with the profiles obtained by incremental fitting method: there the value decreases by 6.7%, whereas here it increases by 12.5%. As can be seen in the graph of integrated emission intensity *vs.* altitude (Fig. 8), this is a consequence of the different peak altitudes found by the two methods. The arguments over which one is more correct require a careful analysis later.

7 FINAL REMARKS

We have demonstrated that the ANN is a promising technique to retrieve volume emission rate profile from rocket photometer measurements in comparison with the incremental straight line fitting method, which is applied most often despite the fact that the altitude of peak emission may be ill-defined.

Even for noisy data or containing gaps, the output profiles provided by ANN are comparable with those derived from methods requiring data be as comprehensive and noiseless as possible, although this does not mean that the ill-conditionedness of the inverse problem has been lifted.

The difficulties are mainly related to the representativity of the dataset, not to the ANN technique itself. After all, the lack of rocket airglow vertical profiles in the equatorial region still persists. As can be seen from the result of generalization test, the rms error between 95.5 km and 100 km suggests that the training subset failed to cover this domain. In order to circumvent this problem, additional geophysical parameters could serve as a quality control by an ANN to validate the synthetic profiles. Within this hypothesis, we would solve the current problem by an ANN cascade.

A comparative analysis with different ANN architectures could be implemented in order to reinforce or refute the alternative result provided by the MLP architecture. This work also illustrates the difficulty of obtaining an inversion method absolutely reliable and universal.

ACKNOWLEDGMENTS

The rocket experiment reported here was undertaken in collaboration with the Brazilian Institute of Aeronautics and Space (IAE/DCTA). We are also grateful to the technical staff of INPE and DCTA. F.C. de Meneses acknowledges support from the Chinese Academy of Science fellowship for young international scientist grant No. 2010Y1GB3 and CAPES scholarship. This work was also partially supported by the following funds: FINEP un-

der contract FINEP-537/CT and CNPq under process 300253/89-3/GM/FV.

REFERENCES

- [1] HARGREAVES JK. 1992. *The Solar-Terrestrial environment*, Cambridge University Press.
- [2] GOMBOSI TI. 2004. *Physics of the space environment*, Cambridge University Press.
- [3] CHAMBERLAIN JW. 1961. *Physics of the Aurora and Airglow*, Academic Press.
- [4] HAIDER SA, KIM J, NAGY AF, KELLER CN, VERIGIN MI, GRINGAUZ KI, SHUTTE NM, SZEGO K & KIRALY P. 1992. Calculated ionization rates, ion densities, and airglow emission rates due to precipitating electrons in the nightside ionosphere of Mars. *Journal of Geophysical Research*, 97: 10637–10641.
- [5] SLANGER TG, COSBY PC, HUESTIS DL & BIDA TA. 2001. Discovery of the Atomic Oxygen Green Line in the Venus Night Airglow. *Science* 291, 5503: 463–465.
- [6] KRASNOPOLSKY VA. 1986. Oxygen emissions in the night airglow of the Earth, Venus and Mars. *Planetary and Space Science*, 34(6): 511–518.
- [7] BURITI RA, TAKAHASHI H & GOBBI D. 2001. First results from mesospheric airglow observations at 7.5°S. *Revista Brasileira de Geofísica*, 19(2): 169–176.
- [8] RAJESH PK, LIU JY, SINHA HSS, BANERJEE SB, MISRA RN, DUTT N & DADHANIA MB. 2007. Observations of plasma depletions in 557.7-nm images over Kavalur. *Journal of Geophysical Research*, 112: A07307.
- [9] GOBBI D, TAKAHASHI H, CLEMESHA BR & BATISTA PP. 1992. Equatorial atomic oxygen profiles derived from rocket observations of OI 557.7 nm airglow emission. *Planetary and Space Science*, 40: 775–781.
- [10] MELO STELLA ML, TAKAHASHI H, CLEMESHA BR, BATISTA PP & SIMONICH DM. 1996. Atomic oxygen concentrations from rocket airglow observations in the equatorial region. *Journal of Atmospheric and Terrestrial Physics*, 58(16): 1935–1942.
- [11] GAO H, XU J & YUAN W. 2005. A Method of Inversing the Peak Density of Atomic Oxygen Vertical Distribution in the MLT Region From the OI (557.7nm) Night Airglow Intensity. *Chinese Journal of Space Science*, 25: 5.
- [12] SHEPHERD G. 2002. *Spectral imaging of the atmosphere*, Academic Press.
- [13] TAKAHASHI H, CLEMESHA BR, SIMONICH DM, MELO STELLA ML, ERAS A, STEGMAN J & WITT G. 1996. Equatorial airglow rocket measurement: MULTIFOT 92 data base. *Journal of Atmospheric and Terrestrial Physics*, 58(16): 1943–1961.

- [14] MURTAGH DP, GREER RGH, McDADE IC, LLEWELLYN EJ & BANTLE M. 1984. Representative volume emission profiles from rocket photometer data. *Annales Geophysicae*, 2: 467–474.
- [15] SISKIND DE & SHARP WE. 1991. A comparison of measurements of the oxygen nightglow and atomic oxygen in the lower thermosphere. *Planetary and Space Science*, 39(4): 627–639.
- [16] CLEMESHA BR & TAKAHASHI H. 1996. Rocket-borne measurements of horizontal structure in the OH(8,3) and Na D airglow emissions. *Advances in Space Research*, 17(11): 81–84.
- [17] ALTINAY O, TULUNAY E, TULUNAY Y. 1997. Forecasting of ionospheric frequency using neural networks. *Geophysical Research Letters*, 24: 1467–1470.
- [18] WINTOFT P & CANDER LJR. 1999. Short-term prediction of foF2 using time-delay neural network. *Physics and Chemistry of the Earth, Part C: Solar, Terrestrial & Planetary Science*, 24(4): 343–347.
- [19] MCKINNELL LA & POOLE WV. 2000. The development of a neural network based short term foF2 forecast program. *Physics and Chemistry of the Earth, Part C: Solar, Terrestrial & Planetary Science*, 25(4): 287–290.
- [20] ZENG Z, HU X & ZHANG X. 2002. Applying artificial neural network to the short-term prediction of electron density structure using GPS occultation data. *Geophysical Research Letters*, 29(9): 35–1.
- [21] NAKAMURA MI, MARUYAMA T & SHIDAMA Y. 2007. Using a neural network to make operational forecasts of ionospheric variations and storms at Kokubunji, Japan. *Earth, Planets and Space*, 59: 1231–1239.
- [22] MCKINNELL LA. 2002. A neural network based ionospheric model for the bottomside electron density profile over Grahamstown, South Africa, PhD. Thesis, Rhodes University, Grahamstown.
- [23] MCKINNELL LA & FRIEDRICH M. 2007. A neural network-based ionospheric model for the auroral zone. *Journal of Atmospheric and Solar-Terrestrial Physics*, 69(12): 1459–1470.
- [24] VANDEGRIFF J, WAGSTAFF K, HO G & PLAUGER J. 2005. Forecasting space weather: Predicting interplanetary shocks using neural networks. *Advances in Space Research*, 36: 2323–2327.
- [25] JANKOVIČOVÁ D, DOLINSKÝ P, VALACH F & VÖRÖS Z. 2002. Neural network-based nonlinear prediction of magnetic storms. *Journal of Atmospheric and Solar-Terrestrial Physics*, 64(5-6): 651–656.
- [26] OZÇELİK R, DIAMANTOPOULOU MJ, BROOKS JR & WIANT HV Jr. 2010. Estimating tree bole volume using artificial neural network models for four species in Turkey. *Journal of environmental management*, 91(3): 742–53.
- [27] YANG Y, TAI NL & YU WY. 2005. ART artificial neural networks based adaptive phase selector. *Electric Power Systems Research*, 76: 115–120.
- [28] ZHANG GP. 2010. Avoiding pitfalls in neural network research. *IEEE Transaction on Systems, Man, and Cybernetics-Part C: Applications and Reviews*, 37 i1. 3–16.
- [29] SHIGUEMORI EH, CHIWIACOWSKY LD, DE CAMPOS VELHO HF & DA SILVA JDS. 2005. An inverse vibration problem solved by an artificial neural network. *TEMA: Tendências em Matemática Aplicada e Computacional*, 6(1): 163–175.
- [30] HAYKIN, S. 1999. *Neural Networks: A Comprehensive Foundation*. Prentice Hall.
- [31] JIMÉNEZ C, ERIKSSON P, MURTAGH D. 2003. First inversions of observed submillimeter limb sounding radiances by neural networks. *Journal of Geophysical Research*, 108(D24): 4791.